PAPER Nr. : 15

# APPLICATION OF 3D EULER CODE TO ROTOR BLADE TIPS

BY

H. STAHL-CUCINELLI

MESSERSCHMITT-BÖLKOW-BLOHM GmbH
MUNICH, GERMANY

**FIFTEENTH EUROPEAN ROTORCRAFT FORUM**

SEPTEMBER 12 - 15, 1989 AMSTERDAM

# APPLICATION OF 3D-EULER CODE TO ROTOR BLADE TIPS

by
H. Stahl-Cucinelli
Messerschmitt-Bölkow-Blohm GmbH, Munich, Germany

## Abstract

A 3D steady Euler code, developed for fixed-wings, has been modified for steady rotor flow conditions.

This code is applied to two different planforms and profiles of rotor blades for steady flow conditions at $\psi = 90^{o}$ and $\mu = 0.34$. The result shows that the planform has a strong influence on the pitching moment distribution and the extension of the supersonic region.

Because the flow is really unsteady for $\mu > 0$, the Euler code was extended to include 3D unsteady flow conditions. Preliminary results are presented for a sinusoidal change of the angle of attack.

For validation the flow of a hovering model rotor is calculated and compared with measurements. The results agree reasonably well with the measurements.

## 1. Introduction

During the last years many efforts have been undertaken to improve the blade tip and reduce transonic effects in fast forward flight. Various tip shapes have been tested in wind tunnel and in flight tests. Because of the high costs there is a strong interest in using computational methods for the design of blade tip shapes.

One of the possibilities for calculating the rotor flow is the solution of the Euler equations by the finite volume method. The derivation of the solution is described in (1). It is available as the so-called EUFLEX-code for 3D steady flow around fixed-wing aircraft. The ROTFLEX developed at the MBB helicopter department is an extension of the EUFLEX to 3D steady rotor flow. The ROTIFLEX is the corresponding 3D unsteady code still under development.

When solving the Euler equations, the grid used has an important influence on the solution itself. Some of these effects are given in (2). For this reason a grid is necessary with high density close to the body surface and a smooth spacial grid structure in the surrounding space. The grid used throughout the calculations

has H-type structure in all coordinate directions, and it is generated by simple analytical functions. The requirement of an analytical grid generator arises from the application to unsteady flow because a grid generator based on an iterative procedure would take too much computational time.

## 2. Comparison of different rotor blade tips

The 3D steady ROTFLEX is applied to two rotor blade planforms as shown in fig.1. These blades have the same radius and chord length as the BO 108 rotor blade. The dimensions of the blade calculated are given below.

| | case A | case B1 | case B2 |
|---|---|---|---|
| radius [m] | 5 | 5 | 5 |
| chord [m] | 0.3 | 0.3 | 0.3 |
| taper ratio | 1.0 | 2/3 | 2/3 |
| twist [deg/m] | -2 | -2 | -2 |
| airfoil | NACA 23012 | NACA 23012 | DM-H4 to 0.8 R<br>from 0.98 R DM-H3 |
| planform | rectangular | tapered from 0.8 to 1.0 R | |

For the calculations 70 percent of the radius are included into the computational domain with the outer boundaries at:

$$-5 \cdot c_o \leqslant x \leqslant 6 \cdot c_o$$
$$0.3 \cdot R \leqslant y \leqslant 1.0 \cdot R + 5 \cdot c_o$$
$$-4 \cdot c_o \leqslant z \leqslant 4 \cdot c_o$$

The resolution of the space is

$$i \times j \times k = 77 \times 62 \times 34 \text{ points}$$

with 29 points on upper and lower side, respectively, fig.2.

The following flight conditions are assumed:

| | |
|---|---|
| forward speed | $v = 75.12$ m/s = 270 km/h |
| advance ratio | $\mu = 0.34$ |
| rotational speed | $\Omega = 43.2\ s^{-1}$ |
| speed of sound | $a = 335$ m/s |
| pitch angle at r = 0 | $\Theta = 8.89$ |

Due to the blade twist the angle of attack and Mach number refered to the blade are:

| | angle of attack | Mach number |
|---|---|---|
| 0.3 R | 5.89° | 0.42 |
| 1.0 R | -1.11° | 0.87 |

For each case 1200 iterations have been performed. The residuum and the aerodynamic coefficients are sufficiently converged.

Fig.3 shows the lift coefficient versus radius. All planforms show a slight dip at about 0.6R. The reason seems to be the set up of the supersonic region on the blade surface, starting on the upper side at about 0.6R and on the lower side further outboard. At the tip the 3D effect becomes dominant and the lift coefficient tends to zero.

The difference of case A and B1 (same airfoil) is the tapering that lowers the $c_L$-distribution towards the tip. It must be the result of 3D interactions because all conditions including the twist are kept constant. The difference on the same planform but different airfoils (NACA 23012 - DM-H4/H3) is caused by the different zero lift angle.

Concerning the moment coefficient a stronger influence of the planform (A - B1) can be seen, fig.4. The tapered blade tip (B1) lowers $c_m$ on the inner radius section but shifts it up close to the tip. The DM-airfoils (B2) show a smaller nose-down $c_m$ compared to B1 all over the radius according to the design targets.

Fig.5a to 5c give the pressure coefficients on the upper side at almost the same radial sections. It can be seen that the tapering lowers the maximum suction peaks, the pressure level and weakens the shock. Immidiately at the tip the shock disappears. Changing the airfoil to DM-H4/H3 again reduces the extension of the supersonic region chordwise and the pressure level as well.

The pressure coefficients on the lower side are given in fig.6a to 6c. It can be seen that especially at the tip the planform reduces suction peaks at the nose significantly independent of the airfoil used.

Fig.7 gives the development of the pressure coefficient due to the influence of the planform and the airfoil at r/R = 0.984. Because of the radial position the lift is negative, the upper side does not show strong shocks. Instead they can be found on the lower side. There are two shocks: one at the leading edge and one on the aft part of the airfoil. The shock at the leading edge is caused by the airfoil cambering because it is designed for positive lift. Changing the planform (A - B1) and then replacing the airfoil (B1 - B2) lowers the pressure coefficient appreciably.

In fig.8 a 3D view of the $c_p$-distribution is given along the span. It can be seen that B1 and B2 have lower pressure coefficients at the tip. The critical pressure coefficient shows that the $c_p$-level is higher on the rectangular blade than on the tapered one.

Fig.9 and 10 show ISO-Mach lines on upper and lower side, respectively. It can be seen that the characteristics of the ISO-lines are mainly dependent on the airfoil used. On the upper side the DM-profiles show very smooth ISO-lines. The NACA 23012 airfoil shows kinks at the Mach lines close to the trailing edge independently of the planform used. This is caused by a small increase of Mach number aft of the shock which is characteristic for the NACA 23012. However, such a phenomenon can also be seen on the lower surface at about $0.5c_o$ for the case B2 (DM-airfoils). Considering case A and B1, the tapered planform reduces the maximum local Mach number on the upper and lower side, as expected.

According to the thickness of the airfoils the planform with DM-profiles has the lowest local $M_{max}$ because of the 9% thick airfoil at the tip. Although it supplies the most negative lift at the tip, the highest local Mach number is smaller than for the other cases.

For further evaluation of the computed data it is of interest to make the extension of the supersonic region on the planforms visible in space, as shown in fig.11. The limiting Mach lines of $M = 1$ are shown in space as a 3D view.

It can be seen that the supersonic region closes towards the tapered tip, for the NACA 23012 as well as for the DM-airfoils, whereas on the rectangular planform it remains open. The difference from the tapered tip with NACA 23012 (B1) to that with DM-airfoils (B2) can be taken from the Mach line of the shock front on the aft part of the airfoil. On the upper side it is steeper for B1 than for B2. The irregularities near the tip seem to be caused by vortices generated at the leading edge where the sweep back begins.

## 3. Comparison with measurements on a hovering model rotor

For the validation of the 3D steady ROTFLEX code, measurements on a hovering model rotor are used (3). The assumption of a 3D steady flow is best fulfilled on a hovering rotor.

The two-bladed untwisted model rotor has a radius of $R = 1.14$ m and a chord of $c_0 = 0.19$ m. The blade is a rectangular one and has a NACA 0012 airfoil. The tip Mach number is chosen to be $M_T = 0.52$. The outer 50% of the radius are included in the computational grid. The resolution of the upper and lower side of the airfoil is 29 points chordwise, respectively. For each collective setting 1200 iterations are performed. The results are sufficiently converged.

For the collective pitch of $\Theta = 0^\circ$ the angle of attack is assumed to be $\alpha = 0^\circ$, as well. In fig.12 the pressure distibutions on upper and lower side, respectively, are shown together with the measurements. Especially in the nose region the measurements compare well with the calculated results.

Investigations for $\Theta \neq 0^\circ$ are necessary taking into account the influence of the tip vortex of the foregoing blade (4).

## 4. First results of 3D unsteady rotor flow

The previous chapters dealt with 3D steady flow solutions. However, when considering a helicopter rotor in forward flight the flow is unsteady and the 3D steady solution only gives a glance of the reality. Therefore the existing 3D steady code was extended to 3D unsteady flow.

For the computation a very rough grid has been used: the resolution of the blade surface was 8 points chordwise and there were only 6 sections along the span. An untwisted rotor blade was assumed with R = 5 m and c = 0.3 m where the outer 25 percent of the span were included in the computational domain.

For test purpose a very simple flow with a hovering tip Mach number of $M_T = 0.6$ is assumed: firstly, the superposition of velocities due to rotational speed and forward motion of the rotor leads to a sinusoidally oscillating Mach number. The advance ratio is $\mu = 0.1$. The angle of attack results from a collective pitch of $\Theta = 1°$, simulated by an inclination of the blade of 1° integrated into the grid. There is no twist and no blade oscillation.

In fig.13 the development of the lift after one cycle and after six cycles is shown. The starting position is $\psi = 0°$. It can be seen that sufficient convergence is achieved after six cycles, because at the beginning $\psi = 0°$ and the end of the cycle $\psi = 360°$ the lift coefficients along radius are almost identical.

Secondly, a test was performed with a sinusoidally oscillating blade but $\mu = 0$. The blade and the grid are the same as above. The oscillating angle of attack ($\Delta\alpha = 1°$) is generated by pitching the blade inside the grid. Thirdly, the two unsteady motions are combined. The results are given for the lift coefficient in fig.14. Again six cycles have been calculated and the solution is assumed to be converged.

Comparing the three cases the influence of only one unsteady parameter and the superposed motion onto the solution can best be observed at $\psi = 90°$ and on the "retreating side" at $\psi = 270°$. Further investigations concerning the grid resolution as well as the pressure and pitching moment coefficients are planned.

## 5. Limits of applications of Euler equations

When calculating real helicopter rotor flow in forward flight the flow seen by the blade is not only 3D unsteady but also partly separated. When looking at the trimmed rotor large angle of attack variations occur, causing blade stall on the retreating side. For calculating the solution of a 3D unsteady flow these large angles have to be handled by the Euler code without getting a breakdown. For this reason a test has been performed with the 3D steady code ROTFLEX for flight conditions taken from chapter 2 for the BO 108 rotor blade, but at $\psi = 270°$. The resulting flight conditions are:

| | angle of attack | Mach number |
|---|---|---|
| 0.3 R | 20.12° | -0.03 |
| 1.0 R | 13.12° | 0.42 |

The large angle of attack and the change of flow direction on the inner blade portion are very delicate flow conditions for an Euler solver. But the computation showed sufficient convergence. When investigating the flow field a strong vortex was found at the tip with small velocities at the center of the vortex. It is shown in

fig.15 for a plane perpendicular to the rotor blade just at the trailing edge. The core of the vortex is marked by an arrow.

This vortex rotates like a solid body. It is an indication of separated flow at the tip forming a vortex on the upper side of the blade. There are indications that this phenomenon is physically meaningful and that if the Euler solution shows separated flow the the flow is indeed separated (5).

Another problem concerning the region of low Mach number is the dependence of the convergence on the Mach number. The higher the Mach number the faster the solution converges. The problem arising is: due to the Mach number distribution along the rotor blade the solution has not the same speed of convergence. With the result that after a certain number of iterations the aerodynamic coefficients are converged at the tip but not at the inner radial portion. Therefore it can happen that the results compare well with measurements only at the tip. Fig.16 shows the qualitative dependence of the number of iterations needed for convergence vs. the local Mach number. Achieving convergence at low Mach numbers is a matter of computational costs.

## 6. Conclusion

A 3D steady Euler code has been applied to rotor blade tip flow. Two different blade planforms with different airfoils have been investigated at typical BO 108 helicopter flight conditions. The results show that the BO 108 planform weakens shocks all along the blade radius compared to a rectangular one. It is also shown that the DM-H4/H3 airfoils are suitable to weaken shocks further and keep the supersonic pressure level low compared to the NACA 23012.

The comparison between computation and measurements on a model rotor shows good agreement for $\Theta = 0^\circ$ and $M_{TIP} = 0.52$. Investigations for $\Theta \neq 0^\circ$ should take into account the influence of the tip vortex of the foregoing blade.

First 3D unsteady calculations show the influence of single and combined unsteady motion of pitching angle and Mach number. For simulating a real rotor flow at fast forward flight, investigations of the capability of calculating the flow at high angle of attack and low tip Mach numbers were performed. The results show that the computation is possible and meanigful.

When computing flows at low Mach numbers on a rotor blade the convergence speed is not constant along blade span. Under certain conditions it may occur that for the inner blade portion a converged solution is not possible. These limits have to be investigated in further studies.

## 7. Literature


1. A. Eberle — MBB-EUFLEX, A new flux extrapolation scheme solving the Euler equations for arbitrary 3D geometry and speed
MBB/LKE122/S/pub/140, 1984

2. H. Stahl — Application of a 3D Euler code to transonic blade tip flow
12th European Rotorcraft Forum, No.29, 1986

3. F.X. Caradonna, C. Tung — Experimental and analytical studies of model helicopter rotor in hover
NASA TM 81232

4. E. Krämer, J. Hertel, S. Wagner — Computation of subsonic and transonic helicopter rotor flow using Euler equations
13th European Rotorcraft Forum, No.14, 1987

5. — Workshop at UniBW Munich, 12.4.1989, on numerical solutions of Euler equations

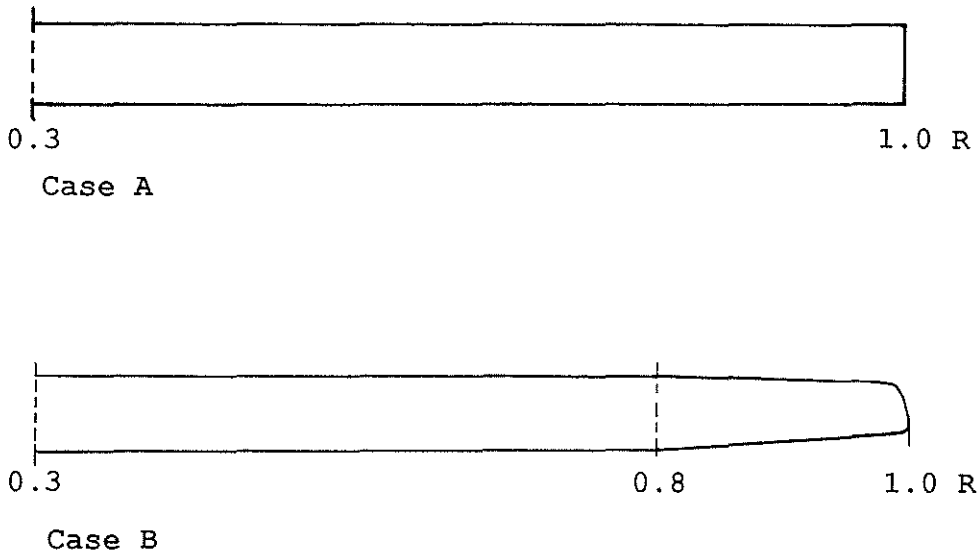


Fig.1 Planforms of the investigated rotor blade, R = 5 m, $c_o$ = 0.3 m, twist = -2°/m, $\tau$ = 2/3

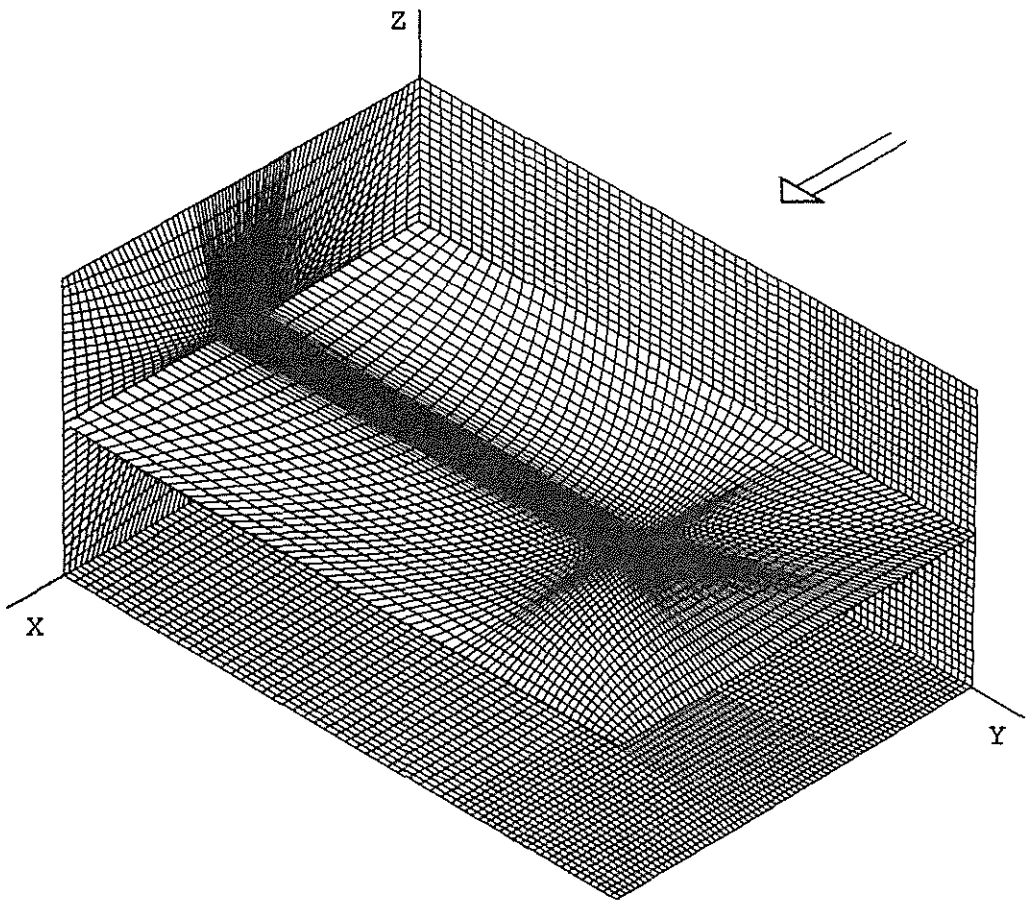


Fig.2 Computational grid shown with the rectangular blade

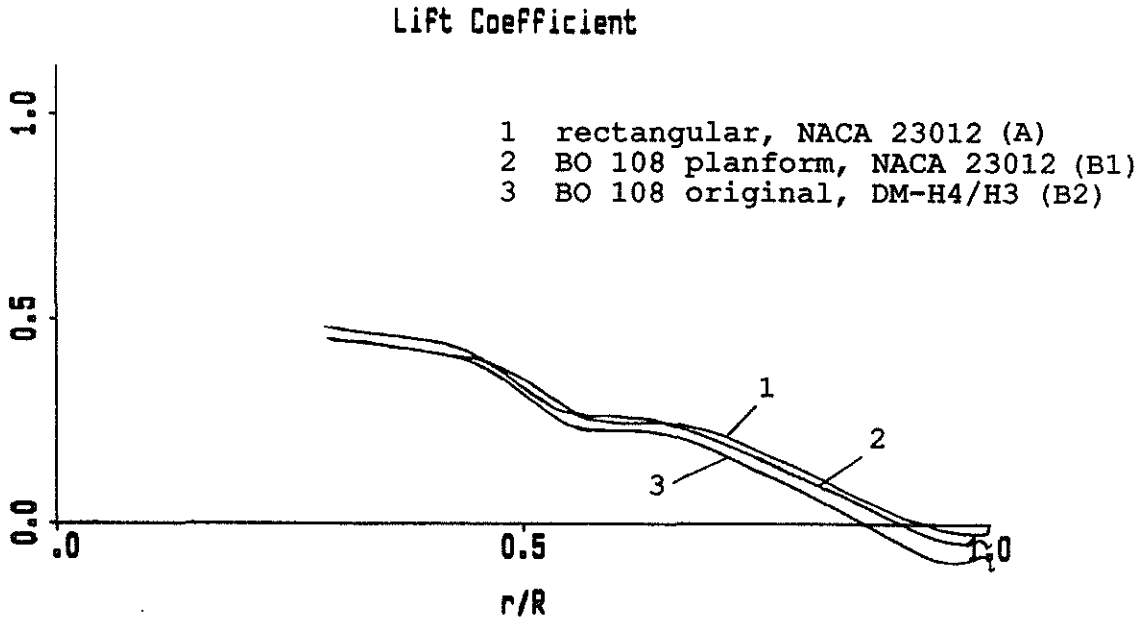


Fig.3 Lift coefficient of the three versions, $M_T$ = 0.87, $\mu$ = 0.34, $\Theta(r=0)$ = 8.89°

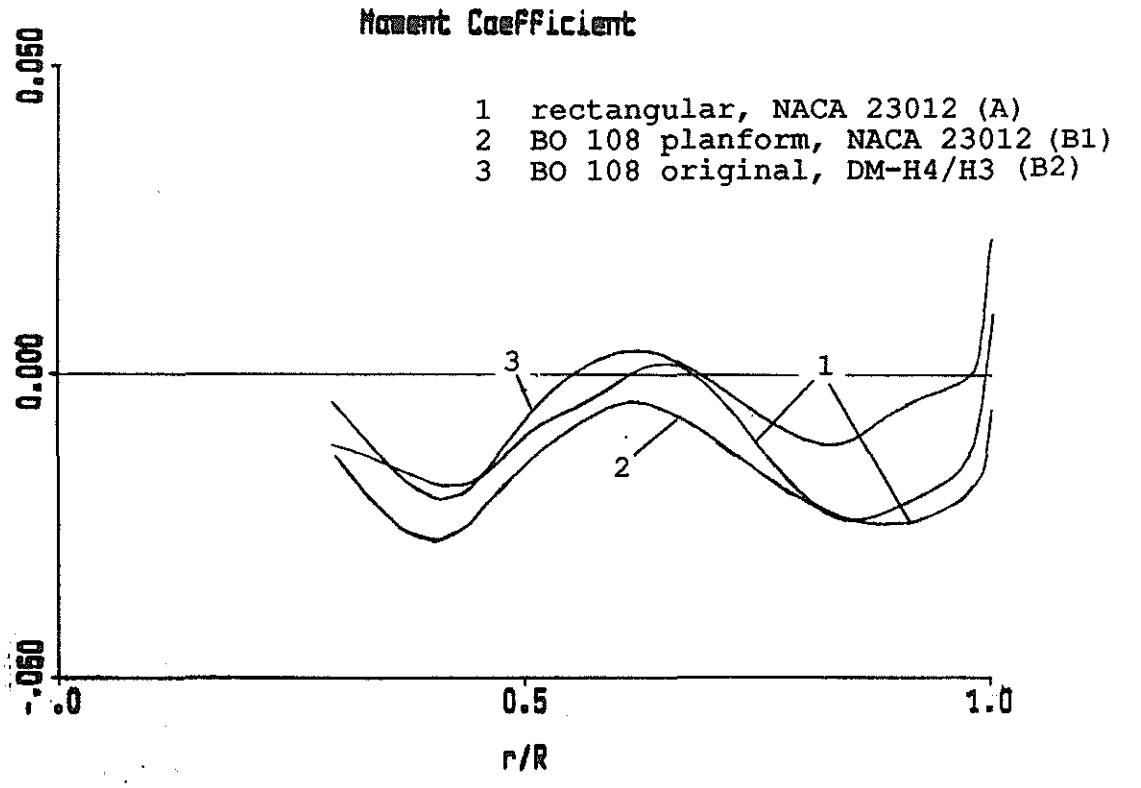


Fig.4 Pitching moment coefficient of the three versions, $M_T$ = 0.87, $\mu$ = 0.34, $\Theta(r=0)$ = 8.89°

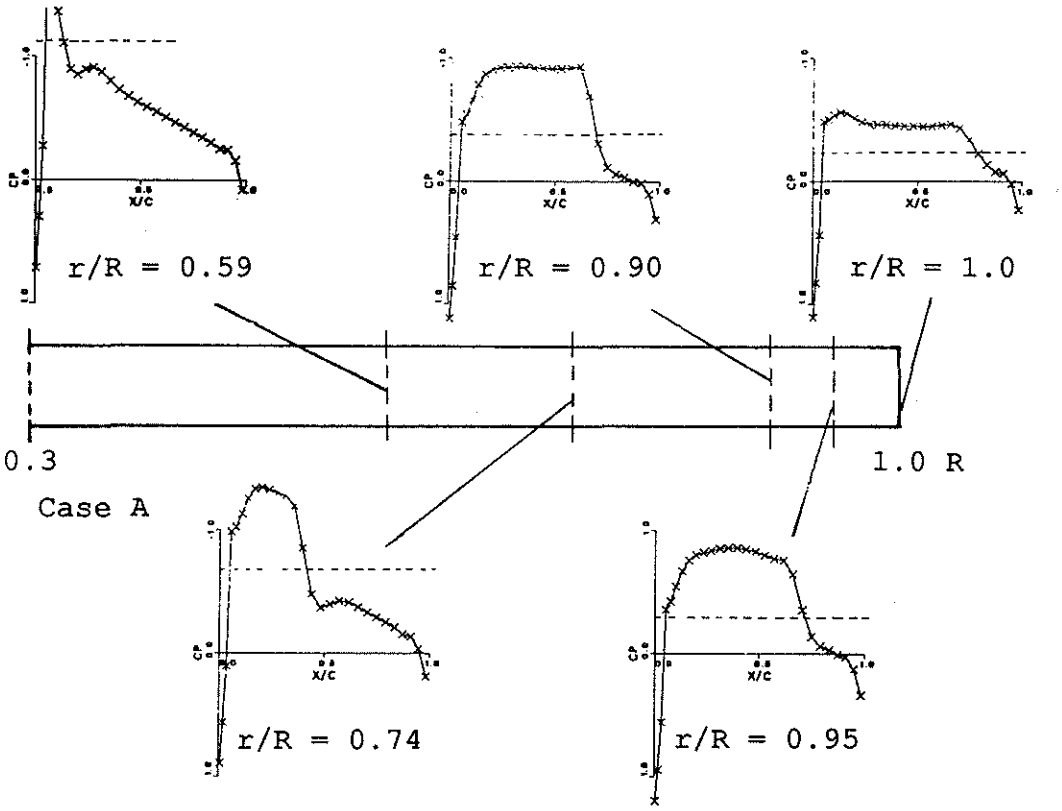


Fig.5a Pressure distributions on the upper side (case A)

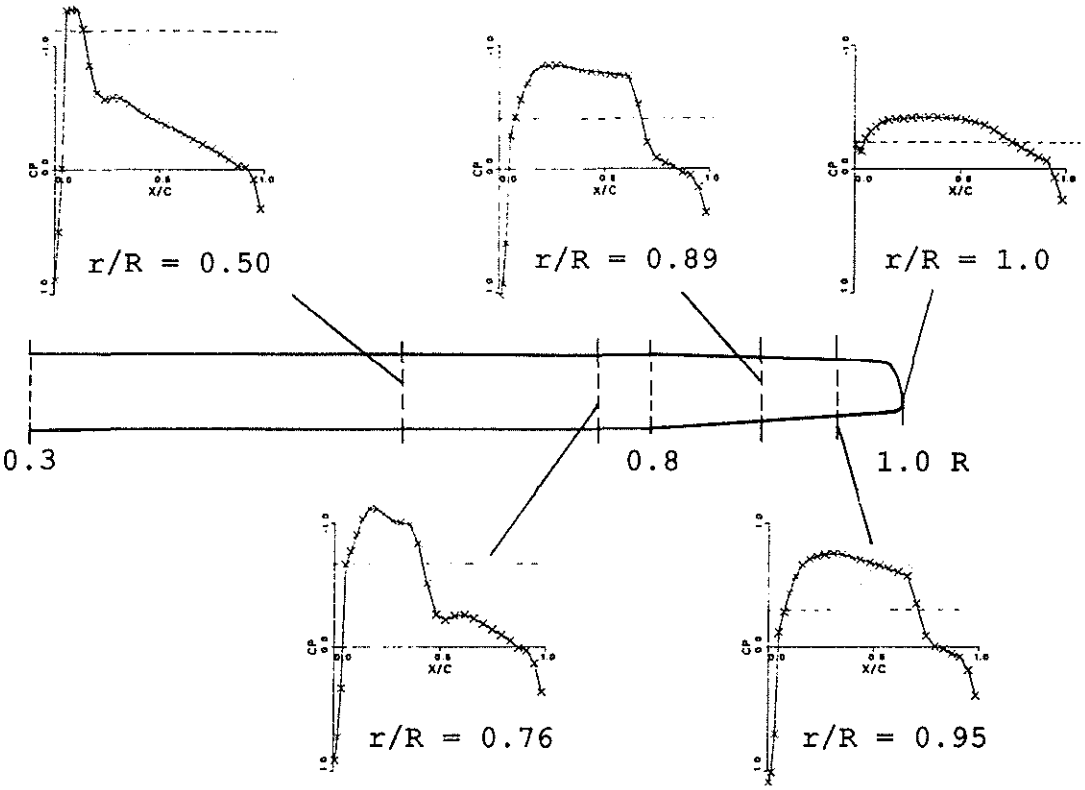


Fig.5b Pressure distributions on the upper side (case B1)

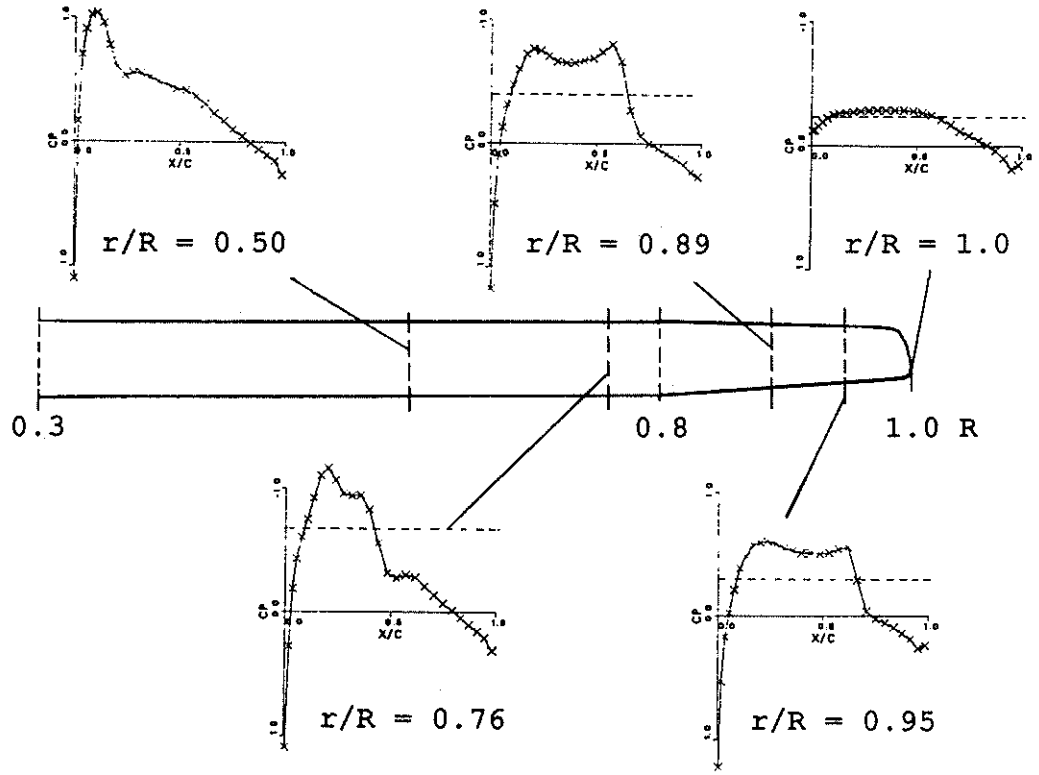


Fig.5c Pressure distributions on the upper side (case B2)

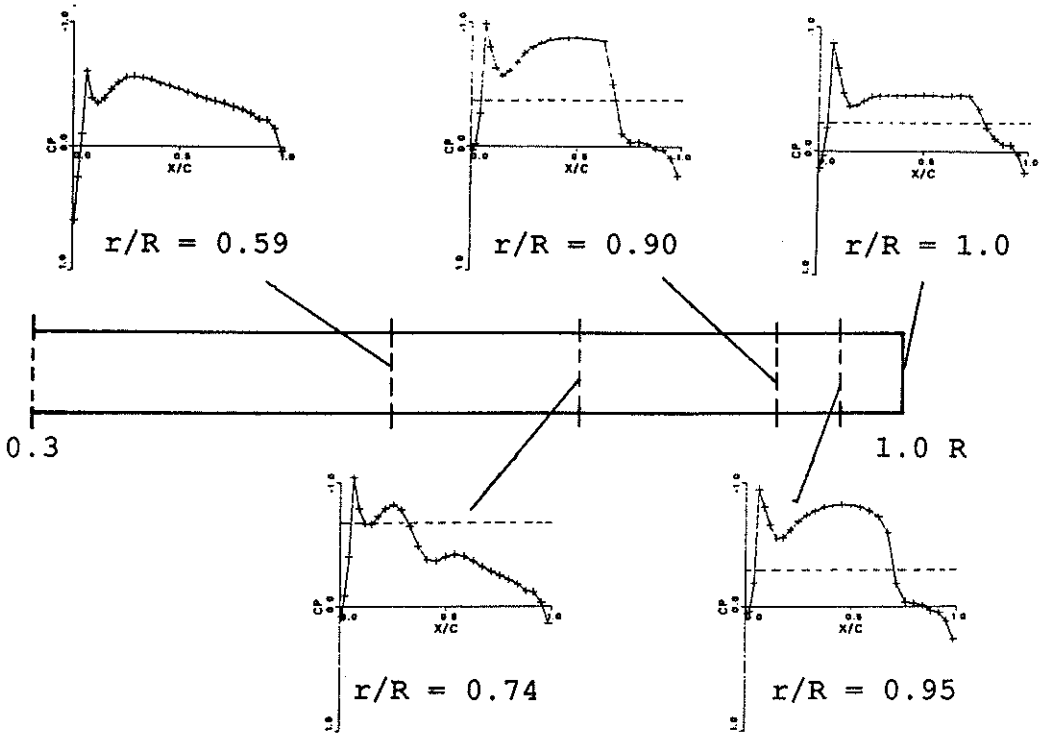


Fig.6a Pressure distributions on the lower side (case A)

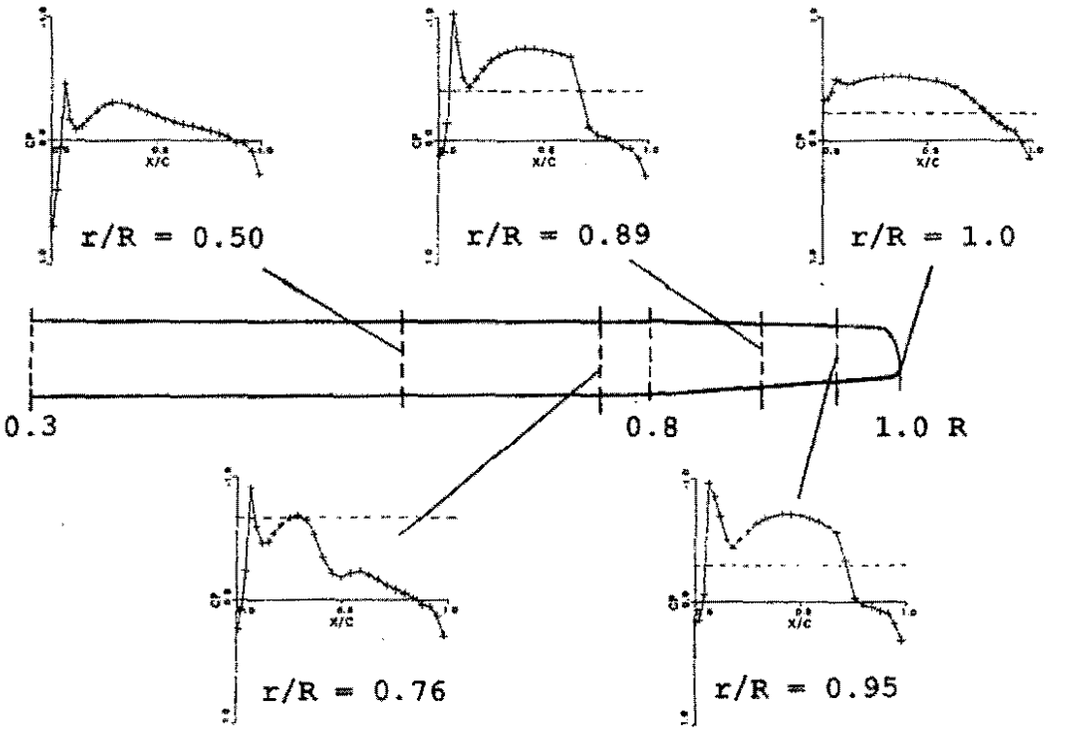


Fig.6b Pressure distributions on the lower side (case B1)

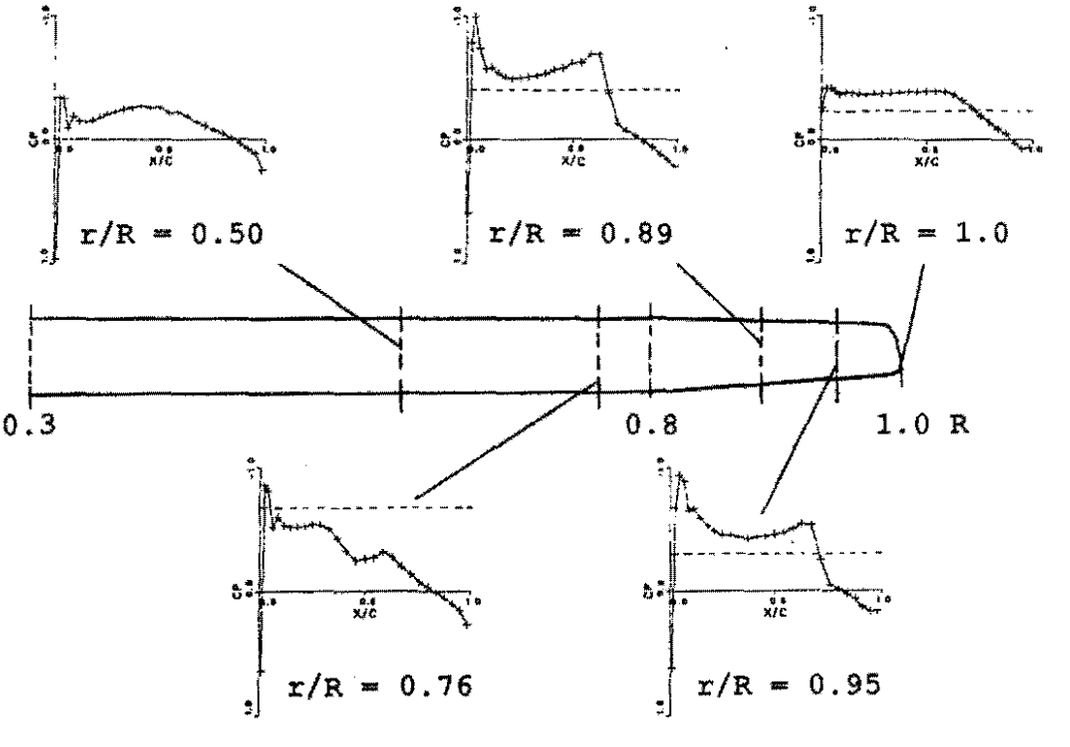


Fig.6c Pressure distributions on the lower side (case B2)

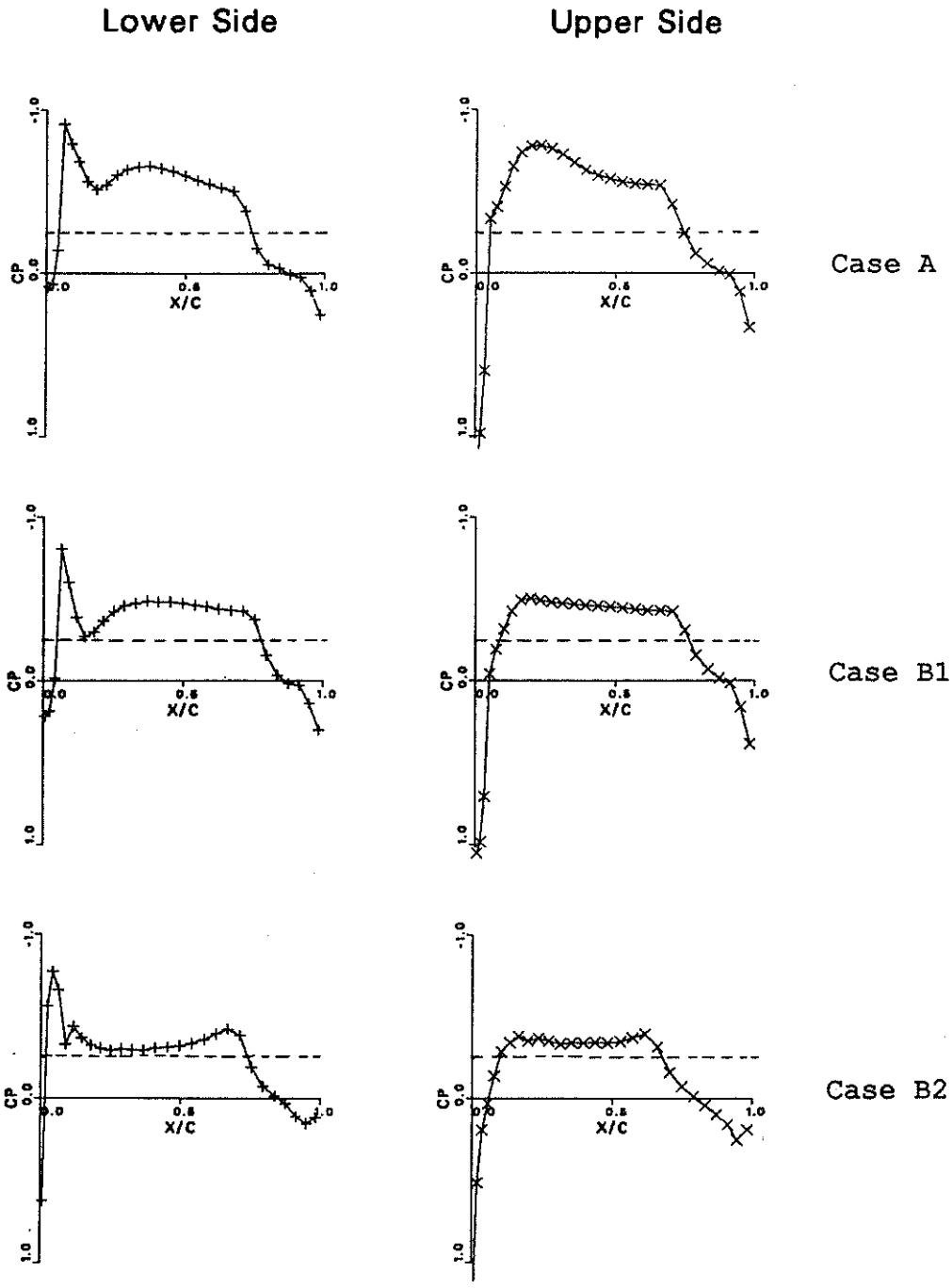


Fig.7 Pressure distribution on upper and lower side, respectively, at r/R = 0.984

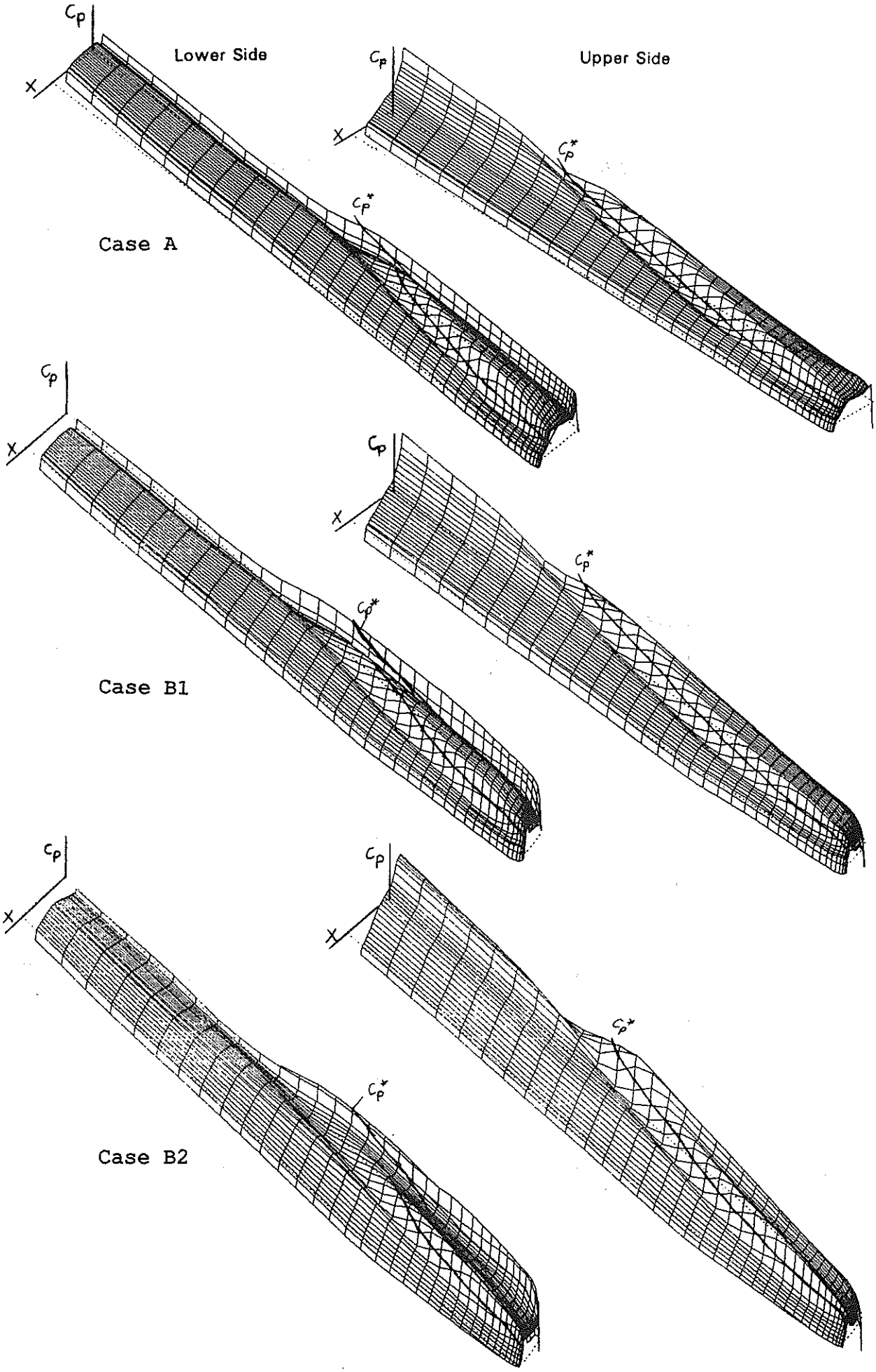


Fig.8 3D view of the pressure distributions on the planform

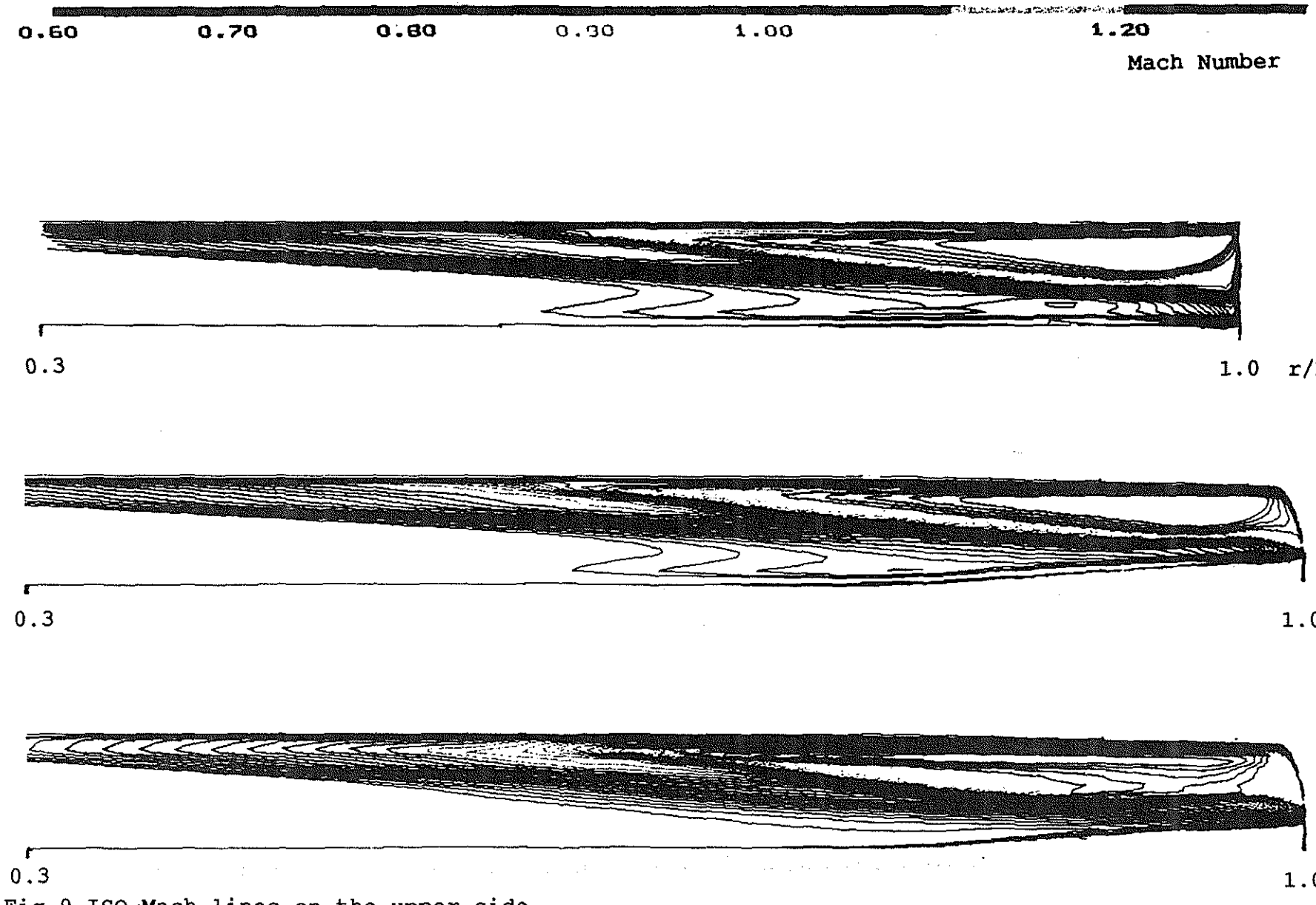


Fig.9 ISO-Mach lines on the upper side

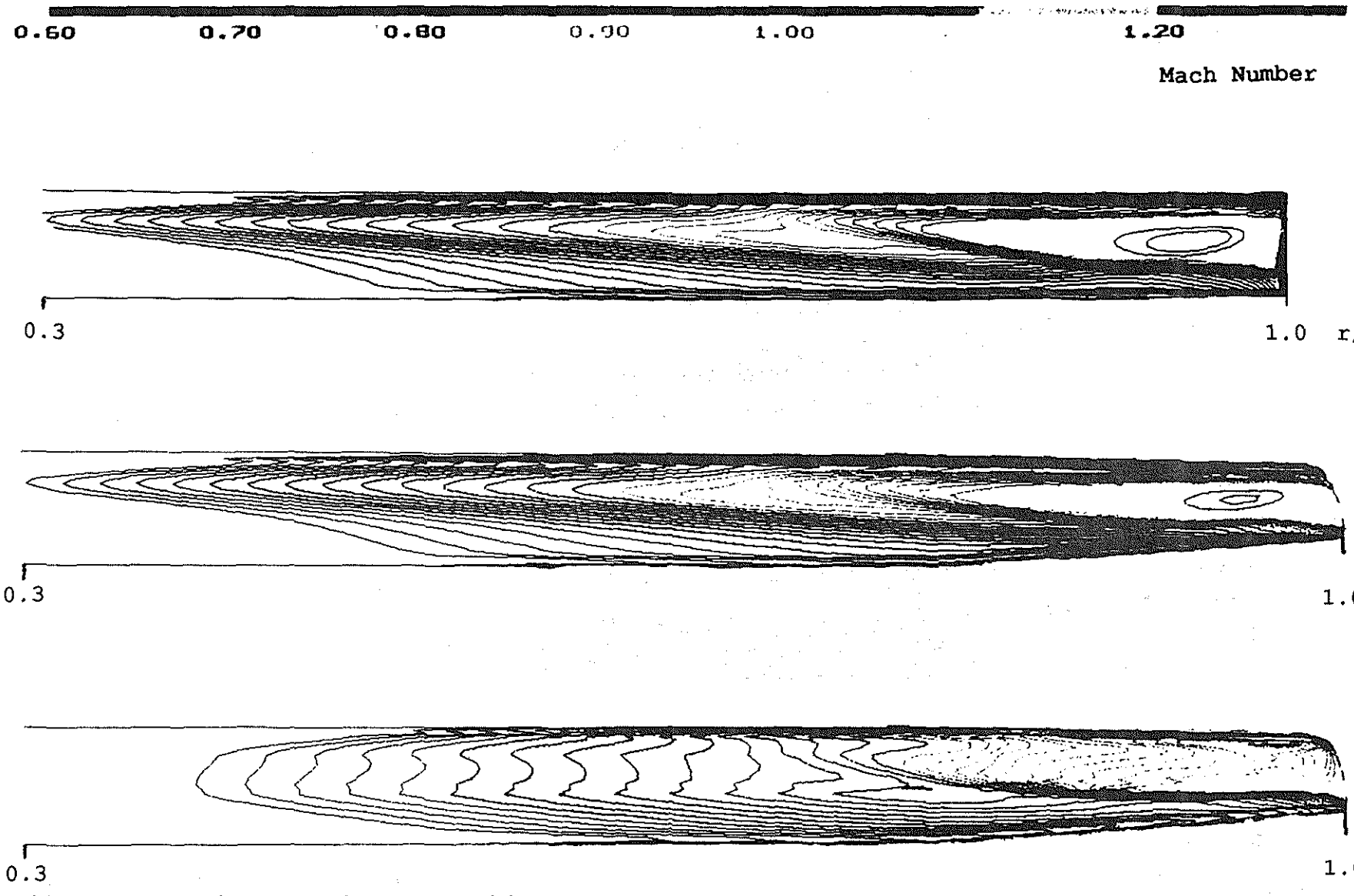


Fig.10 ISO-Mach lines on the lower side

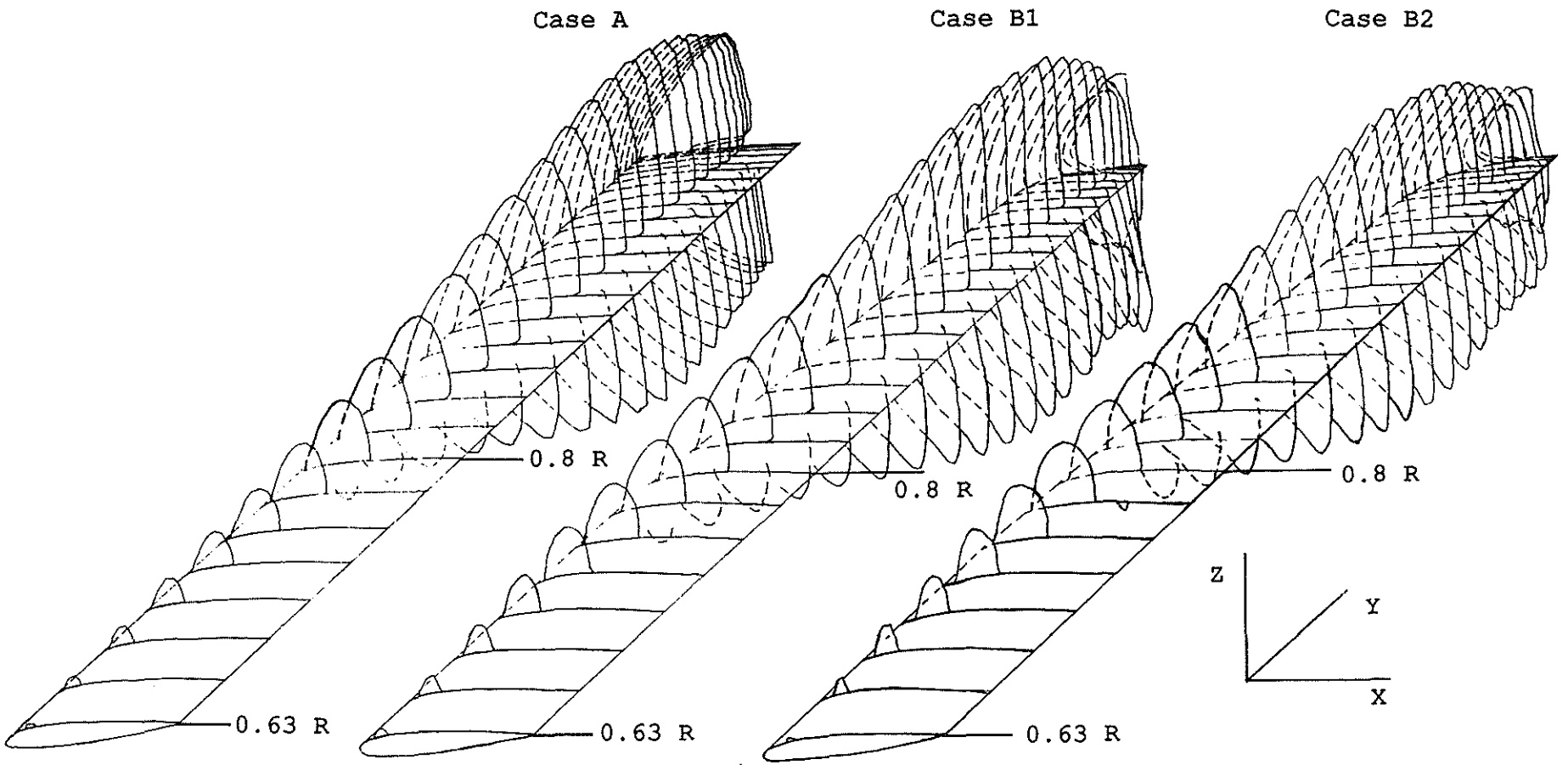


Fig.11 3D view of the M = 1.0 line

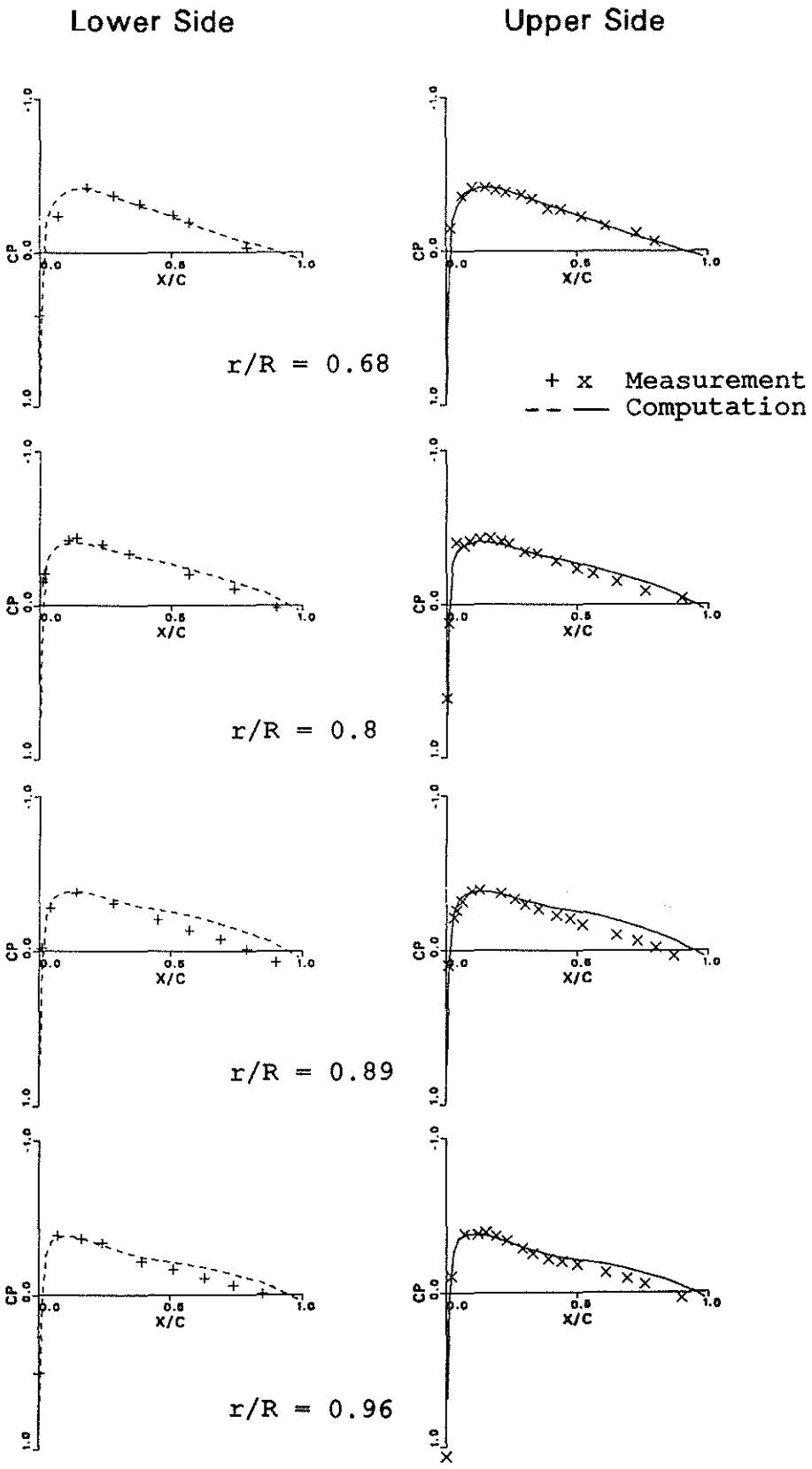


Fig.12 Pressure distributions on a hovering model rotor, M = 0.52, O = 0 , NACA 0012

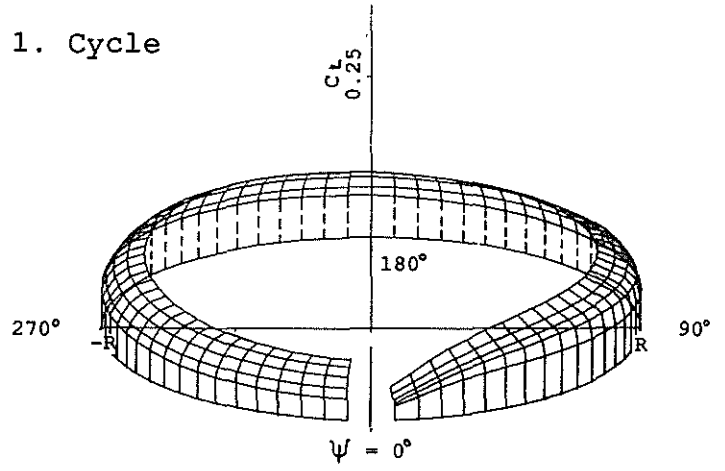


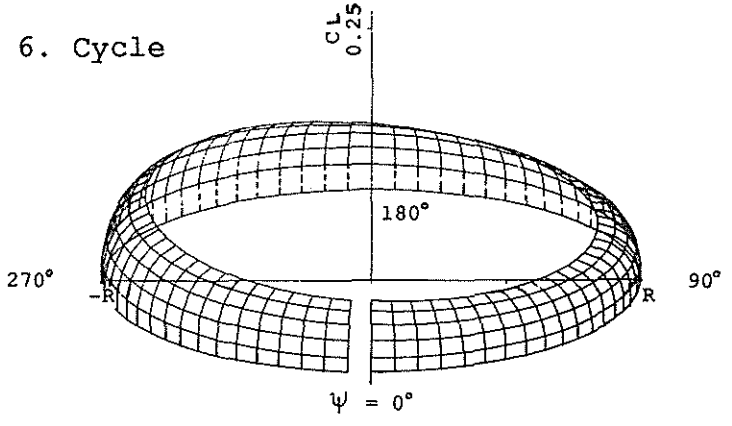


$\alpha_o = 1°$, $\Delta\alpha = 0°$, $\mu = 0.1$

Fig.13 Convergence of unsteady lift coefficients
$\Delta\alpha = 0°$, $\mu \neq 0$

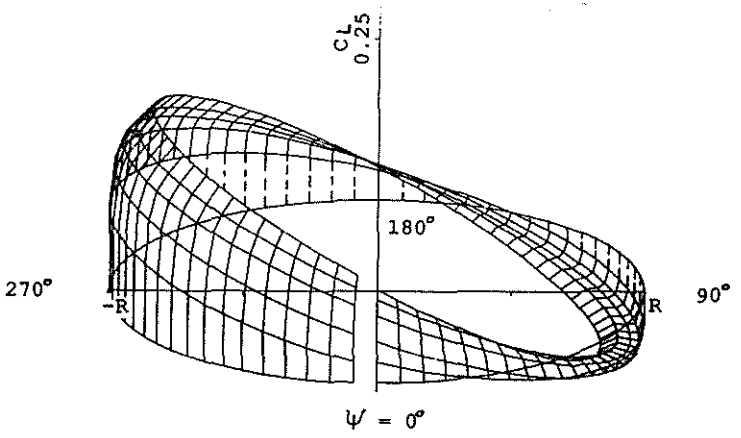


$\alpha_o = 1°$, $\Delta\alpha = 1°$, $\mu = 0$

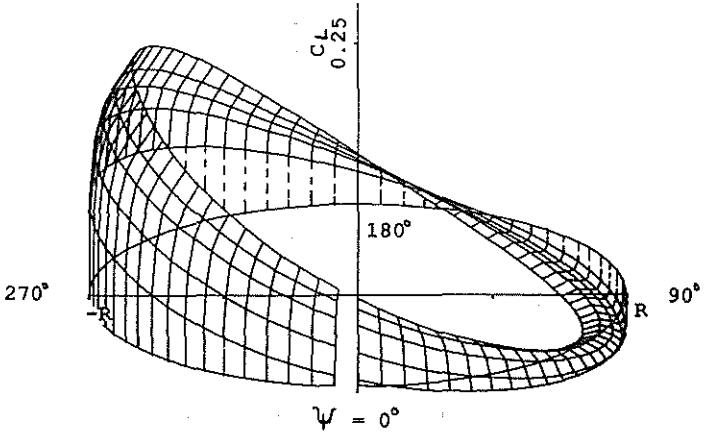


$\alpha_o = 1°$, $\Delta\alpha = 1°$, $\mu = 0.1$

Fig.14 Unsteady lift coefficient for
$\Delta\alpha \neq 0°$, $\mu = 0$ (above)
$\Delta\alpha \neq 0°$, $\mu \neq 0$ (below)

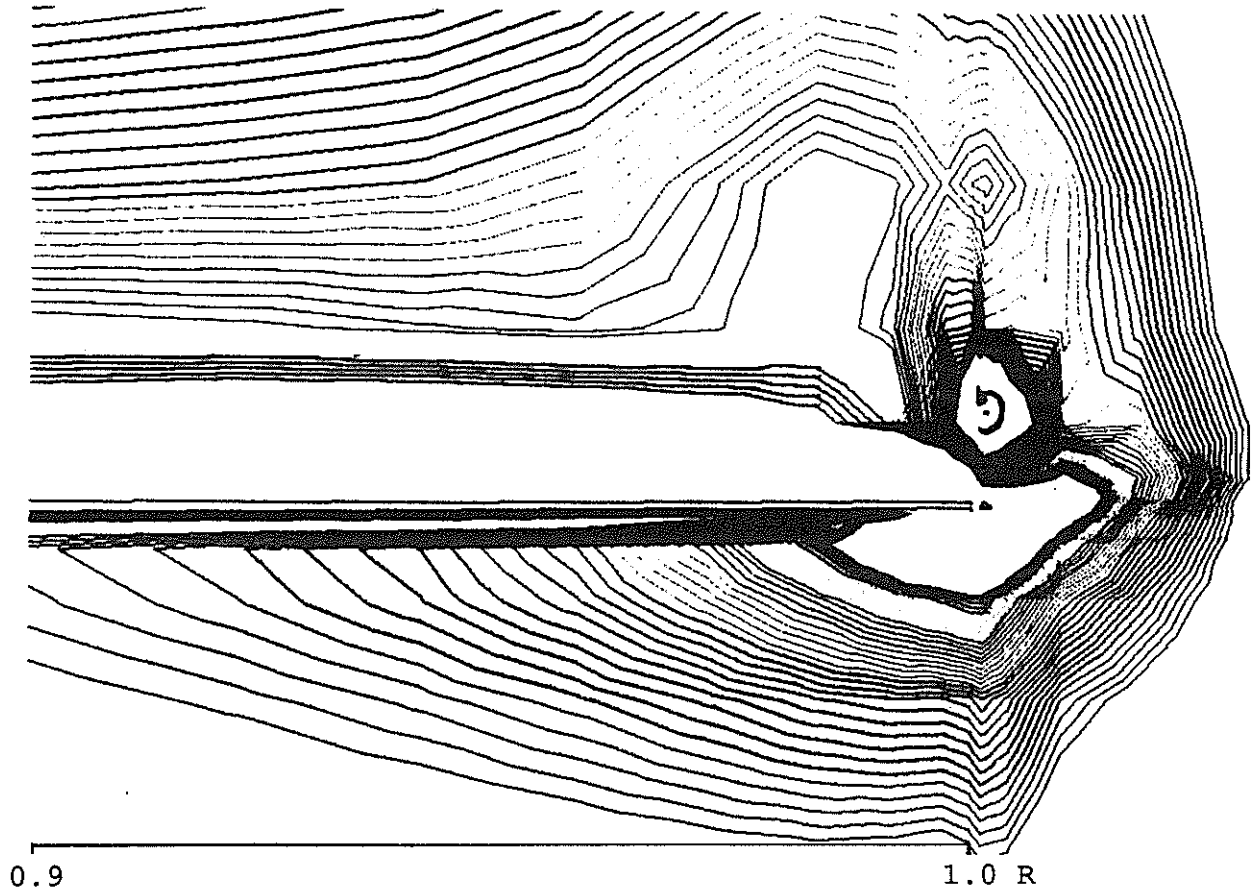


Fig.15 Vortex at the blade tip, $M_T = 0.42$, $\alpha_T = 13.12^\circ$

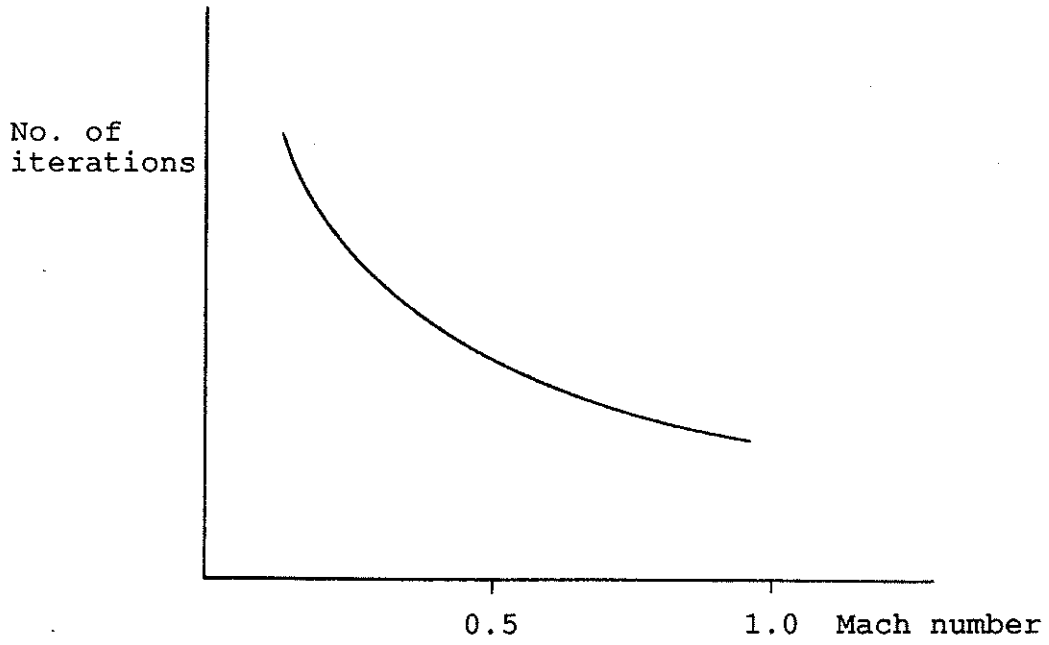


Fig.16 Qualitative dependence of the number of iterations needed for convergence vs. Mach number